J Mater Sci (2011) 46:7415–7422
DOI 10.1007/s10853-011-5704-4

X-ray photoelectron study on $Ba_{0.5}Sr_{0.5}Co_xFe_{1-x}O_{3-\delta}$ (BSCF: $x = 0.2$ and 0.8) ceramics annealed at different temperature and pO_2

Jae-Il Jung · Doreen D. Edwards

Received: 19 January 2011 / Accepted: 7 June 2011 / Published online: 22 June 2011

Abstract X-ray diffraction (XRD) and the X-ray photoelectron spectroscopy (XPS) were measured for the sintered BSCF ceramics ($Ba_{0.5}Sr_{0.5}Co_xFe_{1-x}O_{3-\delta}$, $x = 0.2$ and 0.8: BSCF5528 and BSCF5582, respectively), which were annealed at different temperatures (700 and 950 °C) and gases (O_2 and Ar). The unit cell of the annealed BSCF5528 at 950 °C under Ar expanded by 0.8%, while contracting by 0.45% under O_2. The cubic and rhombohedral phases coexist in the BSCF5582 annealed at 700 °C under O_2. The XPS peak areas of lattice oxygen (O^{2-}) in O_{1s}, ~528 eV, and the shoulder peak of Co_{2p}/Ba_{3d} in BSCF5582 (~778 eV) increased significantly after being annealed in O_2. The areas of the peaks for $BaCO_3$ (87.9/90.2 eV) in Ba_{4d} preferentially were shown to decrease in Ar and increase in O_2.

Introduction

The perovskite $Ba_{0.5}Sr_{0.5}Co_{0.8}Fe_{0.2}O_{3-\delta}$ (BSCF5582) has attracted considerable attention for its applications as a cathode material in intermediate temperature solid oxide fuel cells (IT-SOFCs) and oxygen separation membranes [1, 2]. BSCF as a mixed ionic-electronic conductor (MIEC) exhibits a high oxygen-ionic transport rate via oxygen vacancies, with the oxygen self-diffusion coefficient and ionic conductivity on the order of 10^{-6} cm^2/s and 0.018 S/cm at 700 °C [3]. However, despite its extraordinary conducting properties combined with excellent phase stability at high temperature, the employment of BSCF for real applications is limited by two critical problems: (i) its poor thermomechanical stability with high thermal expansion coefficient (TEC) and (ii) its unstable cubic phase at 800–850 °C at long operation time [4]. As a way of better understanding BSCF for future applications, surface analysis with respect to the changes of B-site cation (cobalt/iron) ratio, temperature and oxygen partial pressure can be used.

The BSCF is widely known to possess a significant amount of oxygen vacancies. Our previous XRD analysis showed that as cobalt concentration (x) increases from $x = 0$ to 0.8 in $Ba_{0.5}Sr_{0.5}Co_xFe_{1-x}O_{3-\delta}$, the lattice constant ($a$) is increased from $a = 3.931$ to 3.986 Å. This change is accompanied by an increase in oxygen vacancies (δ) from $\delta = 0.35$ to 0.40 at room temperature (RT) in air [5]. Also, more oxygen vacancies are formed within the perovskite crystalline structure as temperature increases. There was no significant phase change with increasing cobalt concentration at RT in air, but there is coexistence of cubic and hexagonal BSCF polymorphs, according to Švarcová et al. [6] in the region of 850–900 °C when BSCF5582 is annealed for 10 days in air. McIntosh et al. [7, 8] reported that the cubic perovskite structure of $SrCo_{0.8}Fe_{0.2}O_{3-\delta}$ (SCF) with randomly distributed oxygen vacancies between 600 and 900 °C at $pO_2 = 1$ atm transforms as pO_2 drops below 1 atm and at temperature below 800 °C to a vacancy ordered brownmillerite phase with space group I_{cmm}. The octahedra in the brownmillerite phase are significantly distorted and tilted with an elongated apical bond length relative to the equatorial bond length. This causes an anisotropic thermal expansion, and leads to difficulties in applying SCF as a membrane material. The increased oxygen transport of BSCF over SCF can be explained by two aspects: (i) the rates of oxygen transport in the vacancy disordered cubic perovskite are higher than those

J.-I. Jung (✉) · D. D. Edwards
Kazuo Inamori School of Engineering, Alfred University, Alfred, NY 14802, USA
e-mail: jungji6013@hotmail.com

associated with the brownmillerite phase and (ii) the higher initial oxygen stoichiometries $(3-\delta)$ of BSCF with 2.70 than SCF with 2.48 at RT [8, 9]. However, when larger Ba^{2+} cations are doped into the Sr^{2+} site in SCF the average A–O and B–O bond distances could increase, causing a subsequent destabilization of the higher B-site cation oxidation states [7].

The BSCF is reported to start collapsing at oxygen partial pressure below 10^{-8} atm, because the cobalt ion in perovskite can be reduced to cobalt metal at an oxygen partial pressure lower than 10^{-8} atm, which is accompanied by the deterioration of the perovskite structure and a decrease in oxygen permeability [10–12]. This means that the valence state of the B-site cation, especially cobalt, can influence the perovskite structure stability. According to Pauling's second rule, thermal expansion is enhanced both by the reduction of B site ions into lower valence as well as the decrease in B–O bond strength [10]. Both the high TEC and low chemical stability are closely related with the B-site ions, particularly with cobalt concentration in the BSCF structure, as cobalt ions are easily reduced [13–15]. Therefore, it is meaningful to consider the effect of oxygen vacancy formation on XPS with respect to dopant (Co/Fe ratio) and temperature change, i.e., $[Vo^{\bullet\bullet}]_{dopant}$ and $[Vo^{\bullet\bullet}]_{thermal}$, respectively [16].

Besides unit cell volume expansion with oxygen vacancy formation, the calculated tolerance factor (t_f) increases from 1.042 to 1.052 as cobalt concentration increases from $x = 0$ to 0.8 in $Ba_{0.5}Sr_{0.5}Co_xFe_{1-x}O_{3-\delta}$ according to [17]

$$t_f = \frac{(0.5 \times r_{Ba^{2+}} + 0.5 \times r_{Sr^{2+}} + r_{O^{2-}})}{\sqrt{2}(x \times 0.4 \times r_{Co^{3+}} + x \times 0.6 \times r_{Co^{4+}} + (1-x) \times r_{Fe^{4+}} + r_{O^{2-}})}, \quad (1)$$

where $r_{Ba}^{2+} = 1.61$ Å, $r_{Sr}^{2+} = 1.44$ Å, $r_{Co}^{4+} = 0.53$ Å, $r_{Co}^{3+} = 0.61$ Å, $r_{Fe}^{4+} = 0.59$ Å, $r_{Fe}^{3+} = 0.65$ Å, and $r_{O}^{2-} = 1.40$ Å [18]. Reaney et al. [19] reported that the dielectric permittivity of Ba- and Sr-based perovskite deviates significantly from the referenced temperature values when the tolerance factor (t_f) is between 0.95 and 1.06. This means that the significant deviation of t_f from 1 can cause the crystalline phase to be structurally unstable and give rise to a phase change, which also can be affected by changes in the lattice parameter due to temperature changes, oxygen partial pressure, or dopant ratio (Co/Fe). Such trends for BSCF ($Ba_{0.5}Sr_{0.5}Co_xFe_{1-x}O_{3-\delta}$, $x = 0.2$ and 0.8) were analyzed with XRD and XPS in this study.

Vasquez et al. [20] reported that, as the XPS BE of Ba $4d_{5/2}$ increases from 87.2 to 88.0 eV, the Ba–O bond length linearly increases from 2.802 to 2.818 Å in Tl–cuprate system. This is expected from the Madelung energy. Borca et al. reported that the two main O_{1s} peaks observed in $La_{0.7}Ca_{0.3}MnO_3$ can be assigned to the perovskite structure (i.e., the peak at lower binding energy (528.7–529.0 eV) associated with the O_{1s} of the Mn–O layer, and the peak at 531.0 eV with the O_{1s} of the La/Ca–O) [21–23]. Therefore, the quantitative comparison of XPS BE and peak area will indicate the substantial reaction or bonding state between cations (A-, B-site ions) and anions (O^{2-}, O_2^-/O^-, and CO_3^{2-}).

Generically, the binding energy (BE below) of XPS is expressed as

$$E_b = hv - E_k - \phi \quad (2)$$

where E_b stands for XPS BE (BE below) (eV), h (for XPS radiation energy (eV), E_k for the reflected electron's kinetic energy, and ϕ for work function, $\phi = E_F - E_V$. The BE shift is the chemical shift which changes according to the differences in formal oxidation state, molecular environment, and lattice site. The chemical shift effect can be explained with the charge potential model as shown by:

$$E_i = E_i^o + kq_i + \sum_{i \neq j} \frac{q_i}{r_{ij}} \quad (3)$$

where E_i is the BE of a particular core level on atom i, E_i^o is an energy reference, q_i is the charge on atom i and the final term sums the potential atom at atom i due to "point changes" on surrounding atoms j, also referred to as a Madelung potential [24]. The BE change is the result of a change of valence electron density of q_i which changes the potential inside the sphere by q_i/r_v. For example, a decrease in valence electron density on atom i will cause an increase of BE.

This study dwells on the trend of XPS BE and peak area for the $Ba_{0.5}Sr_{0.5}Co_xFe_{1-x}O_{3-\delta}$ ($x = 0.2$ and 0.8) according to different annealing temperatures ($T = 700$ and 950 °C) and oxygen partial pressures (O_2 and Ar). Unit cell expansion/contraction or phase change for each sample was analyzed with XRD.

Experimental

$Ba_{0.5}Sr_{0.5}Co_xFe_{1-x}O_{3-\delta}$ powders were prepared using a polymerized complex method previously reported in the

literature [25]. The starting materials consist of barium nitrate ($Ba(NO_3)_2$, ≥99.0% purity, Alfar Aesar Co.), strontium nitrate ($Sr(NO_3)_2$, ≥99.0% purity, Aldrich Chemical Co.), cobalt(II) nitrate ($Co(NO_3)_2{\cdot}6H_2O$, ≥99.0% purity, Alfar Aesar Co.), and iron(III) nitrate ($Fe(NO_3)_3{\cdot}9H_2O$, ≥98.0% purity, Alfar Aesar Co.). A 0.04 mol quantity of ethylenediamine tetraacetic acid (EDTA) was mixed with 40 mL of 1 N NH_4OH solution to make NH_4–EDTA buffer solution. Equal molar amounts of barium nitrate (0.01 mol) and strontium nitrate (0.01 mol), x mol (0.004 or 016) of $Co(NO_3)_2{\cdot}6H_2O$ and $(0.02 - x)$ mol of $Fe(NO_3)_3{\cdot}9H_2O$, were added to the buffer solution to make the required stoichiometries of $Ba_{0.5}Sr_{0.5}Co_xFe_{1-x}O_{3-\delta}$ ($x = 0.2$ and 0.8). Anhydrous citric acid (0.06 mol) was added, and the pH value was adjusted to 8 by using a 1 M NH_4OH solution. Each solution was kept on a hot plate at 100 °C and stirred until gelation occurred. After 24 h, the gelled samples were baked in a drying oven at 200 °C for 6 h. The as-produced powders were then calcined at 950 °C for 7 h in air. The synthesized powders were pressed into pellets at 150 MPa and the resulting samples were sintered at 1100 °C for 4 h in air at a heating rate of 4 °C/min. The sintered samples were annealed at 700 and 950 °C for 48 h under the constant flow of 10 mL/min of Ar and O_2 gas within the closed tube furnace, and were cooled down to RT under the same conditions.

For XPS analysis, the sintered bulk samples were cleaved to produce neatly fractured surface by putting samples between sharp blades fastened to a contrived zig and hammering slightly on the top plate. The fastened blades were fixed to the plates and have just enough vertical mobility to cut through the intended spots of the samples without moving horizontally. The fractured samples were inserted into XPS vacuum chamber within 5 min to minimize atmosphere contamination. Samples were placed in the vacuum chamber for 30 h before measurements were taken.

The XPS measurements were performed on a PHI Quantera SXM™ instrument (ULVAC-PHI. Inc., Japan) at a base pressure of 5×10^{-9} Pa using monochromatic Al-Kα radiation (1486.6 eV). The analyzer pass energy was set to 26 eV for narrow scans, the step size of which was 0.05 eV. The number of sweeping was 2 and the ratio to noise was 50. The spot size of the energy beam on the sample was ~100 μm. The shifts in energy (charging) of the XPS spectra were corrected using the C_{1s} peak at 284.6 eV as a reference peak.

The crystal structures of the sintered samples were analyzed by X-ray diffraction, using a Siemens D5000 diffractometer using Cu-Kα radiation, a scan range of 20°–120°, a step size of 0.02°, and a counting time of 8 s. Lattice parameters were determined using a least-squares method.

Result

Figure 1 shows the XRD data for (a) $Ba_{0.5}Sr_{0.5}Co_{0.2}Fe_{0.8}O_{3-\delta}$ (BSCF5528) and (b) $Ba_{0.5}Sr_{0.5}Co_{0.8}Fe_{0.2}O_{3-\delta}$ (BSCF5582) samples which were annealed for 48 h at 700 and 950 °C under Ar and O_2 gases. When compared with the sintered sample, the overall annealed BSCF5528 samples maintain the cubic perovskite structure. Significant expansion was seen at 0.8% under Ar, while contraction was seen at 0.45% under O_2, as summarized in Table 1. On the other hand, BSCF5582 expands and contracts relatively less with 0.2 and 0.17%, respectively (as shown in Fig. 1 and Table 1). In particular, Fig. 1b shows that BSCF5582 annealed at 700 °C under O_2 possesses a coexistence of the cubic and rhombohedral phases. Kriegel and Preub [26, 27] suggested that higher oxygen partial pressure could favor hexagonal phase formation in BSCF5582 because the hexagonal perovskite very often possesses a higher oxygen stoichiometry than the cubic phase with the same cationic composition. Compared with BSCF5528, BSCF5582 is expected to absorb more oxygen into its perovskite structure, because it keeps a higher concentration of oxygen vacancies [16, 25]. In addition, because it has a higher tolerance factor, ($t_f = 1.06$), BSCF5582 is more prone to structural distortion upon the uptake of oxygen into the perovskite structure under high oxygen pressure, resulting in the coexistence with rhombohedral symmetry at 700 °C as shown in Fig. 1b.

Figure 2 shows the XPS spectra of Fe_{3p} and Co_{3p} for annealed BSCF5528 and BSCF5582 samples, in comparison with the samples sintered in air. The BE of BSCF5528 shows little change in O_2, while there is a significant change in both BEs of Fe_{3p} and Co_{3p} in Ar, especially for Fe_{3p} BE (54.3 eV) in Ar at 950 °C. This implies that the unit cell thermal expansion can affect the BE of B-site cations in the BSCF5528 perovskite structure, but with only a slight change in O_2. Figure 2b shows the BE peak shifts of BSCF5582 under both annealing conditions (Ar and O_2). Specifically, the peak shift for O_2 annealed at 700 °C is noticeable when compared with BSCF5528 in Fig. 2a.

Figure 3 shows the XPS spectra of O_{1s} for BSCF5528 and BSCF5582. In BSCF5528, the BE of lattice oxygen (O^{2-}) shows systematic increases from 527.9 eV in O_2 at 950 °C to 528.3 eV in Ar at 950 °C as shown in Table 2. The normalized area was calculated as a ratio for each corresponding peak area. In Fig. 3 and Table 2, the peak areas of BSCF5528 are relatively well distributed in O^{2-}, O_2^-/O^-, and CO_3^{2-}/OH^-. However, the BE of lattice oxygen (O^{2-}) in BSCF5582 changes according to annealing conditions, showing a noticeable increase for the spectrum in O_2. This indicates that BSCF5582 has a significant amount of oxygen uptake within the lattice under

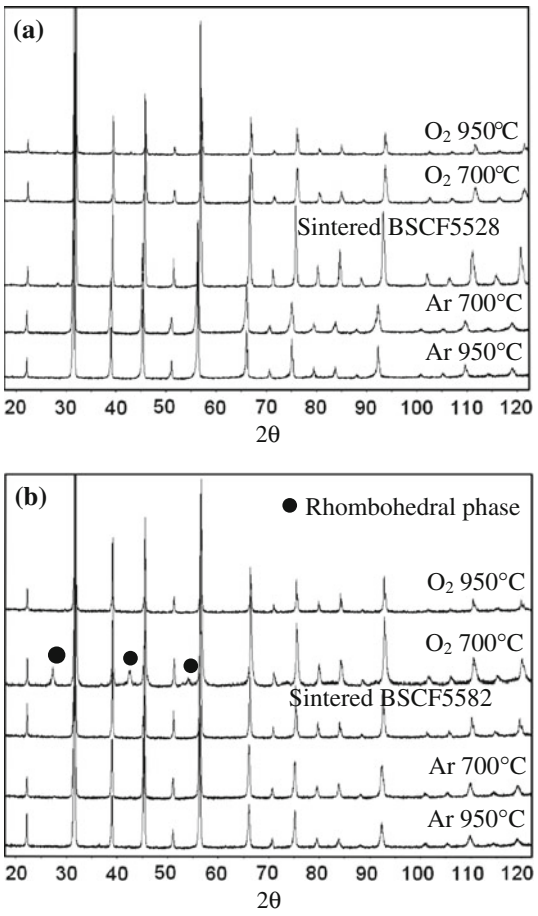

Fig. 1 The XRD data of **a** $Ba_{0.5}Sr_{0.5}Co_{0.2}Fe_{0.8}O_{3-\delta}$ (BSCF5528) and **b** $Ba_{0.5}Sr_{0.5}Co_{0.8}Fe_{0.2}O_{3-\delta}$ (BSCF5582) annealed at 700 °C and 950 °C under O_2 and Ar

oxidation conditions, enough to lead to structural distortion at 700 °C, as shown in the XRD data of Fig. 1. The peak areas of O^{2-} in BSCF5528 under Ar are reduced significantly.

The general trend in the peak shifts of Co_{2p}/Ba_{3d} shown in Fig. 4 are quite similar to the peaks of O_{1s} shown in Fig. 3. The particular increase of the shoulder peak area (~778 eV) of BSCF5582 annealed in O_2 shown in Fig. 4b matches with those peaks (~528 eV) in O^{2-} of O_{1s} BSCF5582 shown in Fig. 3b, the trend of which can be more quantitatively compared in Tables 2 and 3. This signifies that the shoulder peak at ~778 eV is another type of Ba XPS peak (Ba_{2d}) which comes from the interrelation between Ba cation and oxygen anion.

Figure 5 shows the XPS spectra of Ba_{4d} for BSCF5528 and BSCF5582. In Fig. 5a, BSCF5528, the overall peaks shift to a higher BE as samples are reduced, which is similar to the behavior of the O_{1s} peak in BSCF5528, as shown in Fig. 3a. When the BaO peaks represented by 89.2/92.2 eV and the $BaCO_3$ peak areas represented by

Table 1 Summary of lattice parameter and expansion rate (%) for $Ba_{0.5}Sr_{0.5}Co_xFe_{1-x}O_{3-\delta}$ ($x = 0.2$ and 0.8) samples

Samples	BSCF5528		BSCF5582	
	a (Å)	Exp (%)	a (Å)	Exp (%)
O_2, 950 °C	3.941	−0.51	3.98	−0.15
O_2, 700 °C	3.945	−0.40	3.98	−0.20
Sintered samples	3.961	–	3.98	–
Ar, 700 °C	3.993	0.81	3.99	0.2
Ar, 950 °C	3.994	0.83	3.99	0.2

87.9/90.2 eV are compared, the peak areas of $BaCO_3$ preferentially decrease in Ar, and increase in O_2, as summarized in Table 4. This implies that BSCF5528 uptakes oxygen preferentially into $BaCO_3$ bonds under oxidation, and loses oxygen preferentially from $BaCO_3$ bonds under reduction. The peak changes of BSCF5582 according to oxidation/reduction shown in Fig. 5b are too irregular and hinder substantial analysis, probably due to the great intake of oxygen into oxygen lattice sites.

Discussion

Under oxidation conditions for BSCF5582, there was significant uptake of oxygen within the perovskite structure as shown in O_{1s} and Co_{2p}/Ba_{3d}. This can be attributed to the high oxygen non-stoichiometry (δ) within the BSCF5582 structure, which is considered to enable the structure to take more oxygen into oxygen sites. In combination with the high oxygen intake, the high t_f in BSCF5582 can distort the perovskite structure, as shown by the co-existence of rhombohedral and cubic phase at 700 °C under O_2 in the XRD data of Fig. 1b. Such a phase change was not observed at 950 °C in O_2 for BSCF5582, which is in agreement with the report of Švarcová et al. [6]. This phenomenon can be explained by the significantly higher unit cell volume expansion at 950 °C, approximately 50% higher than at 700 °C for BSCF5582 [25]. The expanded unit volume can play the role of alleviating the structural distortion that comes from the uptake of oxygen into oxygen lattice in O_2.

The effect of interrelation between Ba and O is also observed in both the BE areas of ~778 eV (Ba_{3d}) and 528 eV (O_{1s}), which increased significantly in O_2. Therefore, we are able to suggest two possibilities for the identity of the BE at ~778 eV: (i) another oxidation state of Ba_{3d} and (ii) the secondary shoulder peak of Ba_{3d}, but it is not yet clear which assumption is more plausible. However, this study makes it clear that ~778 eV comes from the interrelation between Ba and O.

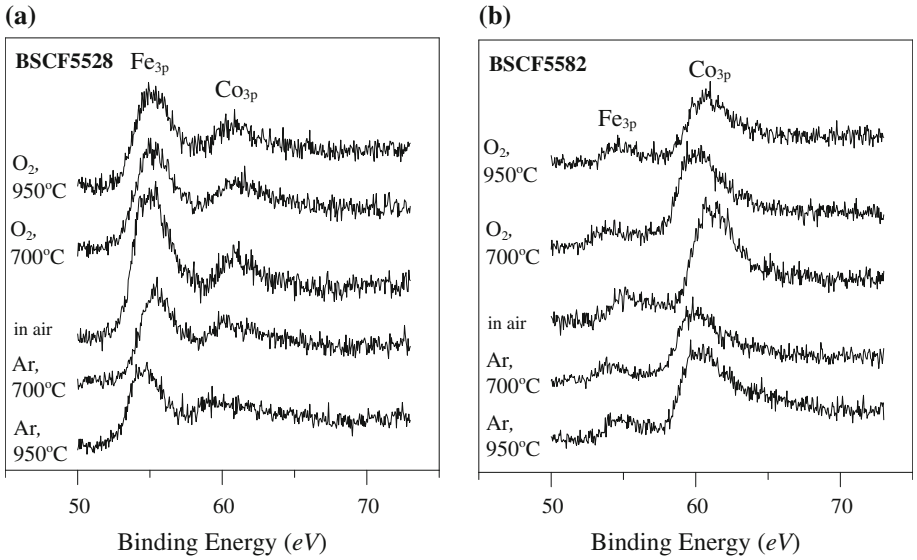

Fig. 2 The XPS spectra of Fe_{3p} and Co_{3p} for the fractured surfaces of sintered **a** BSCF5528 and **b** BSCF5582 annealed at 700 and 950 °C under O_2 and Ar

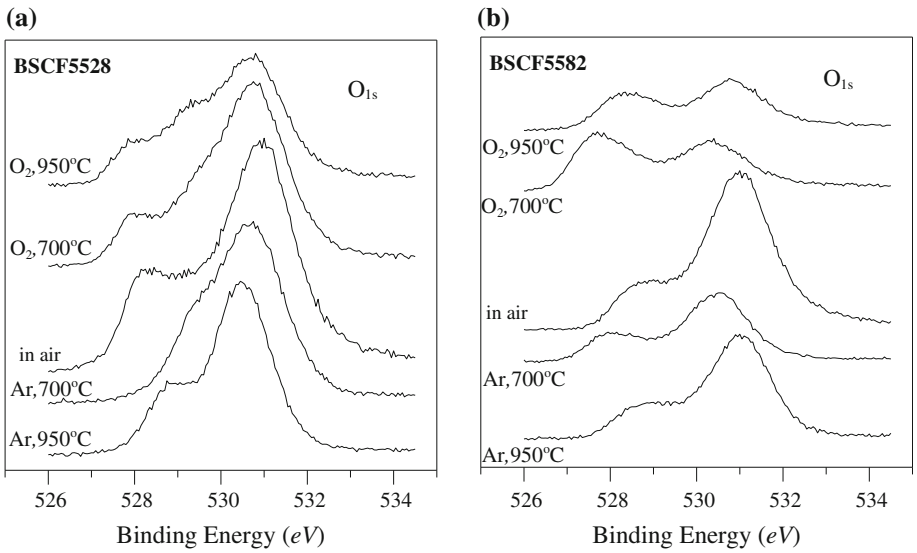

Fig. 3 The XPS spectra of O_{1s} for the fractured surfaces of sintered **a** BSCF5528 and **b** BSCF5582 annealed at 700 and 950 °C under O_2 and Ar

Table 2 Deconvoluted results of O_{1s} for $Ba_{0.5}Sr_{0.5}Co_xFe_{1-x}O_{3-\delta}$ ($x = 0.2$ and 0.8) XPS spectra

	BE (eV)			Area			Normalized area		
	O^{2-}	O_2^-/O^-	CO_3^{2-}/OH^-	O^{2-}	O_2^-/O^-	CO_3^{2-}/OH^-	O^{2-}	O_2^-/O^-	CO_3^{2-}/OH^-
O_2, 950 °C	527.9	529.1	530.7	466	992	3233	0.10	0.21	0.69
O_2, 700 °C	528.1	529.3	530.85	610	813	4594	0.10	0.14	0.76
As-sintered BSCF5528	528.1	529	530.9	722	1382	5460	0.10	0.18	0.72
Ar, 700 °C	528.6	529.3	530.66	218	616	4475	0.04	0.12	0.84
Ar, 950 °C	528.3	528.9	530.48	214	695	3679	0.05	0.15	0.80
O_2, 950 °C	528.3	529	530.81	646	418	1737	0.23	0.15	0.62
O_2, 700 °C	527.9	528.8	530.38	841	87	1093	0.42	0.04	0.54
As-sintered BSCF5582	528.5	529.2	530.96	633	548	5987	0.09	0.08	0.84
Ar, 700 °C	527.9	528.7	530.47	372	301	2242	0.13	0.10	0.77
Ar, 950 °C	528.3	529.1	531	262	855	3414	0.06	0.19	0.75

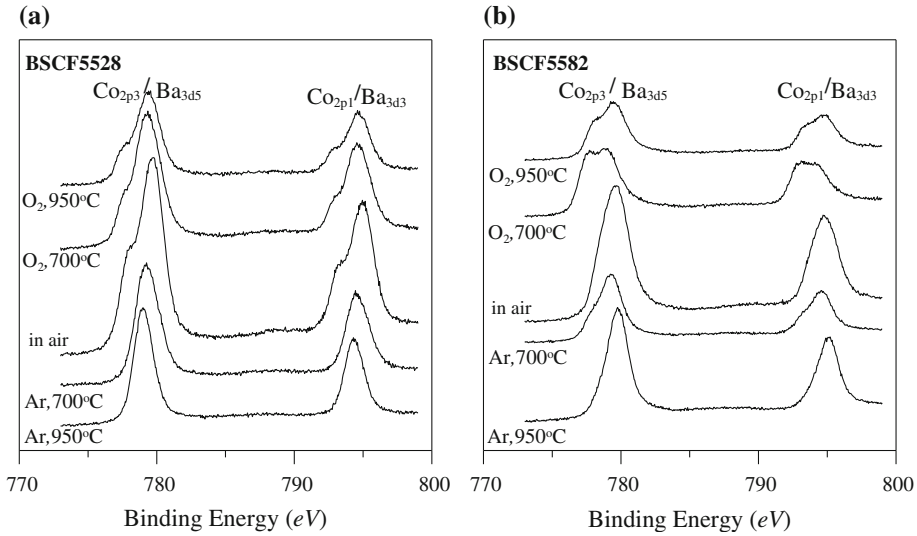

Fig. 4 The XPS spectra of Co_{2p}/Ba_{3d} for the fractured surfaces of sintered **a** BSCF5528 and **b** BSCF5582 annealed at 700 and 950 °C under O_2 and Ar

Table 3 Deconvoluted results of Co_{2p}/Ba_{3d} for $Ba_{0.5}Sr_{0.5}Co_xFe_{1-x}O_{3-\delta}$ ($x = 0.2$ and 0.8) XPS spectra

	BE (eV)		Area		Normalized area	
	~778 eV	780.1 eV	~778 eV	780.1 eV	~778 eV	780.1 eV
O_2, 950 °C	777.47	779.34	283	1614	0.15	0.85
O_2, 700 °C	777.62	779.46	320	2172	0.12	0.88
As-sintered BSCF5528	777.84	779.67	1060	1294	0.23	0.77
Ar, 700 °C	778.94	779.35	1342	242	0.09	0.91
Ar, 950 °C	778.7	779.1	1137	185	0.12	0.88
O_2, 950 °C	777.9	779.44	1064	5470	0.16	0.84
O_2, 700 °C	777.38	778.81	1698	6572	0.21	0.79
As-sintered BSCF5582	778.33	779.57	693	13579	0.05	0.95
Ar, 700 °C	777.72	779.23	683	5804	0.11	0.89
Ar, 950 °C	778.28	779.75	644	9131	0.07	0.93

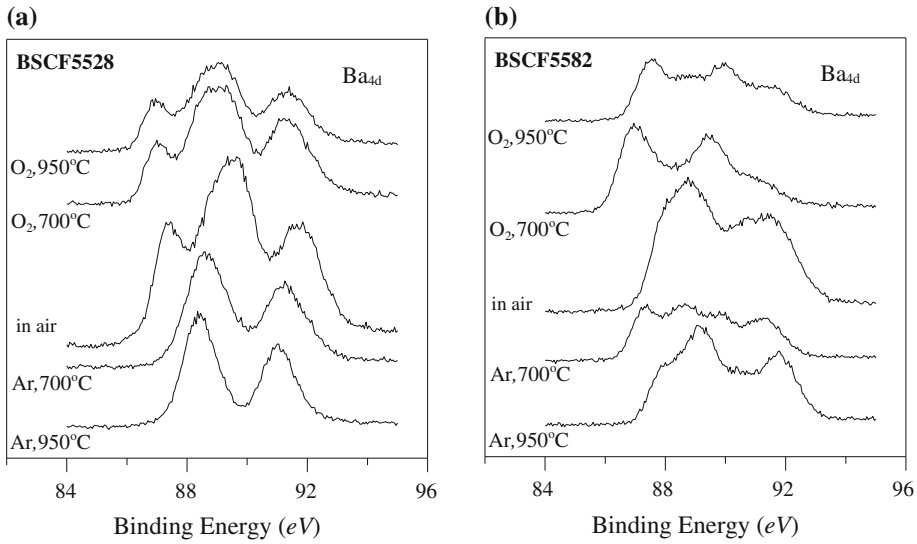

Fig. 5 The XPS spectra of B_{4d} for the fractured surfaces of sintered **a** BSCF5528 and **b** BSCF5582 annealed at 700 and 950 °C under O_2 and Ar

Table 4 Deconvoluted results of Ba_{4d} for $Ba_{0.5}Sr_{0.5}Co_xFe_{1-x}O_{3-\delta}$ ($x = 0.2$ and 0.8) XPS spectra

	BE (eV)				Area			
	87.9 eV	89.2 eV	90.2 eV	92.4 eV	87.9 eV	89.2 eV	90.2 eV	92.4 eV
O_2, 950 °C	86.9	88.91	90.9	91.5	283	1614	51	617
O_2, 700 °C	86.95	88.93	90.9	91.5	320	2172	37	876
As-sintered BSCF5528	87.39	88.77	89.75	91.71	1060	1294	1626	1580
Ar, 700 °C	88.56	89.52	91	91.7	1342	242	687	434
Ar, 950 °C	88.35	89.14	90.9	91.5	1137	185	724	263
O_2, 950 °C	87.52	88.64	89.9	91.5	618	359	724	418
O_2, 700 °C	86.99	88.8	89.7	91	899	1170	453	280
As-sintered BSCF5582	88.11	89.08	90.35	91.56	1089	1337	601	1495
Ar, 700 °C	87.38	88.54	89.7	91.2	518	493	527	561
Ar, 950 °C	88.01	89.2	90.5	91.8	557	1187	410	885
	BE (eV)				Normalized Area			
	87.9 eV	89.2 eV	90.2 eV	92.4 eV	87.9 eV	89.2 eV	90.2 eV	92.4 eV
O_2, 950 °C	86.9	88.91	90.9	91.5	0.11	0.63	0.02	0.24
O_2, 700 °C	86.95	88.93	90.9	91.5	0.09	0.64	0.01	0.26
As-sintered BSCF5528	87.39	88.77	89.75	91.71	0.19	0.23	0.29	0.28
Ar, 700 °C	88.56	89.52	91	91.7	0.50	0.09	0.25	0.16
Ar, 950 °C	88.35	89.14	90.9	91.5	0.49	0.08	0.31	0.11
O_2, 950 °C	87.52	88.64	89.9	91.5	0.29	0.17	0.34	0.20
O_2, 700 °C	86.99	88.8	89.7	91	0.32	0.42	0.16	0.10
As-sintered BSCF5582	88.11	89.08	90.35	91.56	0.24	0.30	0.13	0.33
Ar, 700 °C	87.38	88.54	89.7	91.2	0.25	0.23	0.25	0.27
Ar, 950 °C	88.01	89.2	90.5	91.8	0.18	0.39	0.13	0.29

In BSCF5528, the BE of lattice oxygen (O^{2-}) shows a systematic increase from 527.9 eV in O_2 at 950 °C to 528.3 eV in Ar at 950 °C, as shown in Fig. 3a and Table 2, which matches with the unit cell expansion of the XRD data in Fig. 1a. On the other hand, the generic BE of CO_3^{2-}/OH^- decreases in reducing conditions.

Because bonding between the cation and CO_3^{2-}/OH^- is more stable than that between the cation and O^{2-} in reduction conditions [28], it is expected that more CO_3^{2-}/OH^- is adsorbed to the cation sites, while O^{2-} is deficient in oxygen lattice sites. This can explain the shift of CO_3^{2-}/OH^- to lower BE, while O^{2-} shifts to higher BE under reduction conditions. In addition to Madelung potential, as shown in Eq. 3, the work function, ϕ, as shown in Eq. 2, can possibly contribute to the BE peak shift. This is because the B-site cations are reduced in the reduction condition. The increased work function, ϕ, can cause the BE peak shift of CO_3^{2-}/OH^- for O_{1s} to the lower BE under reduction (Ar at 700 °C and Ar at 950 °C) in Fig. 3. However, a more detailed study is needed to explain this phenomenon.

The preferential uptake of oxygen into $BaCO_3$ bonds under oxidation and loss of oxygen out of $BaCO_3$ in BSCF5528 under reduction (as illustrated in Fig. 5) explains the hump number change from three to two as the BSCF structure loses oxygen.

Conclusions

When BSCF samples (BSCF5528 and BSCF5582) were annealed at different temperatures ($T = 700$ and 950 °C) and atmospheres (O_2 and Ar), it was possible to observe the simultaneous effects of Co/Fe ratio change ($[V_O^{\bullet\bullet}]_{dopant}$), temperature ($[V_O^{\bullet\bullet}]_{thermal}$) and oxygen partial pressure (pO_2) on XPS and XRD. The dramatic trends of XPS spectra, O_{1s}, Co_{2p}/Ba_{3d} and Ba_{4d} were explained through oxygen non-stoichiometry (δ), t_f, and phase or crystal unit cell change in XRD analysis.

For BSCF5582 under oxidizing conditions, there was significant uptake of oxygen in the oxygen lattice sites, as shown in O^{2-} of O_{1s} and ~778 eV of Co_{2p}/Ba_{3d} of the XPS spectra. BSCF5582 underwent phase changes at 700 °C in O_2, because of its high oxygen non-stoichiometry (δ) as well as its high t_f. The uptake of oxygen in the oxygen lattice sites can contribute to the cramped spacing

between Ba and O in BSCF5582, which in turn will cause structural distortion and phase changes. This argument also supports the idea that ~778 eV of Co_{2p}/Ba_{3d} of XPS comes from the interrelation between Ba and O in that both the BE areas of ~778 eV (Ba_{3d}) and 528 eV (O_{1s}) increased significantly in O_2. At high temperature, 950 °C, the significant unit cell volume expansion can alleviate structure distortion caused by oxygen uptake.

The preferential uptake and loss of oxygen in $BaCO_3$ (Ba_{4d}) of BSCF5528 explain the peak number changes from three to two as the BSCF structure loses oxygen on the fractured sample surface.

Acknowledgements The author kindly acknowledges the insightful discussions of Dr. Robert A Condrate.

References

1. Shao Z, Halle SM (2004) Nature 431:170. doi:10.1038/nature02863
2. Shao Z, Yang W, Kong Y, Dong H, Tong J, Xiong G (2000) J Membr Sci 172:177
3. Bucher E, Egger A, Ried P, Sitte W, Holtappels P (2008) Solid State Ion 179:1032
4. Efimov K, Xu Q, Feldhoff A (2010) Chem Mater 22:5866
5. Jung JI, Misture ST, Edwards DD (2010) Solid State Ion 181:1287
6. Švarcová S, Wiik K, Tolchard J, Bouwmeester HJM, Grande T (2008) Solid State Ion 178:1787
7. McIntosh S, Vente J, Haije W, Blank D, Bouwmeester H (2006) Chem Mater 18(8):2187
8. McIntosh S, Vente JF, Haije WG, Blank DHA, Bouwmeester HJM (2006) Solid State Ion 177(9–10):833
9. McIntosh S, Vente J, Haije W, Blank D, Bouwmeester H (2006) Solid State Ion 177(19–25):1737
10. Zeng P, Chen Z, Zhou W, Gu H, Shao Z, Liu S (2007) J Membr Sci 291(1–2):148
11. Hendriksen P, Larsen P, Mogensen M, Poulsen F, Wiik K (2000) Catal Today 56(1–3):283
12. Shao Z, Yang W, Cong Y, Dong H, Tong J, Xiong G (2000) J Membr Sci 172(1–2):177
13. Kostogloudis GC, Fertis P, Ftikos C (1998) J Eur Ceram Soc 18(14):2209
14. Chen Z, Ran R, Zhou W, Shao Z, Liu S (2007) Electrochim Acta 52(25):7343
15. Zhu Q, Jin T, Wang Y (2006) Solid State Ion 177(13–14):1199
16. Jung JI, Misture ST, Edwards DD (2009) J Electroceram 24:261. doi:10.1007/s10832-009-9567-x
17. Liu BW, Zhang Y, Tang L (2009) Int J Hydrogen Energy 34:435
18. Shannon R (1976) Acta Crystallogr Sect A Cryst Phys Diffr Theor Gen Crystallogr 32(5):751
19. Reaney IM, Colla EL, Setter N (1994) Jpn J Appl Phys 33:3984
20. Vasquez RP, Siegal MP, Overmyer DL, Ren ZF, Lao JY, Wang JH (1999) Phys Rev B 60(6):4309
21. Borca CN, Canulescu S, Loviat F, Lippert T, Grolimund D, Döbeli M, Wambach J, Wokaun A (2007) Appl Surf Sci 254:1352
22. Beyreuther E, Grafström S, Eng LM, Thiele C, Dörr K (2006) Phys Rev B 73:155425
23. Choi JW, Zhang J, Liou SH, Dowben PA, Plummer EW (1999) Phys Rev B 59(20):13453
24. Briggs D, Seah MP (1983) Practical surface analysis by Auger and x-ray photoelectron spectroscopy. John Wiley & Sons, New York, p 119
25. Ovenstone J, Jung JI, White JS, Edwards DD, Misture ST (2008) J Solid State Chem 181:576
26. Kriegel R, Preub N (1996) Thermochim Acta 285:91
27. Kriegel R, Kircheisen R, Töpfer J (2010) Solid State Ion 181:64
28. Kingery WD, Bowen HK, Uhlmann DR (1976) Introduction to ceramics, 2nd edn. John Wiley & Sons, New York, p 414